Fabrication update on non-contact mirror slumping technology for the International X-ray Observatory mirrors

Abdul Mohsen Al Husseini, Ralf K. Heilmann, Mark L. Schattenburg,

Space Nanotechnology Laboratory, MIT Kavli Institute for Astrophysics and Space Research, Massachusetts Institute of Technology, Cambridge, Massachusetts 02139, USA

ABSTRACT

A method of thermally shaping individual sheets of glass for the International X-Ray Observatory using porous mandrels as air bearings has been developed, which eliminates the problems of sticking and dust particle-induced distortion which plague traditional slumping methods. A detailed mathematical model of the process has been developed, allowing prediction of final glass shape based on process parameters that include air supply pressure, imperfections on the mandrel surface, glass total thickness variations and gravity vector orientation. Experiments to verify model findings are conducted under closed-loop control of pressure and apparatus tilt. Little improvement in repeatability is seen, suggesting that the error is due to unmodeled forces such as contact forces from the glass holding technique. Finally, the design process and fabrication of a third generation slumping tool is presented. In addition to scaling the design to accomodate larger flats, slumps are done horizontally to float the glass and minimize contact during the process. New capabilities of the tool include active gap measurement and control, as well as plenum air temperature monitoring.

Keywords: x-ray optics, slumping, air-bearing, non-contact

1. INTRODUCTION

Flat glass sheets with high surface quality are in demand for applications ranging from flat panel displays to x-ray telescope optics. Since commercially available glass sheets of < 1 mm thickness typically have a surface waviness on the order of hundreds of microns, strict figure requiements make it challenging to utilize progressively thinner sheets. In the case of the proposed International X-ray Observatory (IXO), a collection area of 3 m^2 is required at a resolution of only 5 arcsec in order to resolve distant and faint objects. Due to the large collection area, payload restrictions limit the areal density of the glass to 50 gm/cm^3, 50 times smaller than Chandra and 8 times smaller than XMM.[1] Over the past decade, much research has been devoted to producing glass sheets that can meet IXO performance requirements. The two main approaches considered for IXO are glass slumping and silicon pore optics, adopted by NASA Goddard Space Flight Center and the European Space Agency respectively. While both techniques show promise, they suffer from inherent drawbacks that may prevent obtaining a satisfactory surface.

Conventional glass slumping is performed by placing a flat glass substrate over a refractory mandrel of the desired shape, and elevating the temperature so that the softened glass may conform to the shape of the mandrel. While simple in principle, the presence of dust particles on the mandrel causes mid-range frequency errors on glass figure. Conversly, thorough cleaning of the mandrels causes sticion due to the absence of dust particles that serve as spacers between both parts. Given these issues, a slumping tool was developed that relied on air bearings with the aim of eliminating the issues with dust particles and stiction altogether rather than working around them.[2,3] In this process, glass sheets are placed between a pair of micro-porous ceramic air bearings ground to sub-micron flatness, as shown in Figure 1a. Mandrel faces are spaced apart by a distance 10-100 μm larger than glass thickness, resulting in a 5-50 μm-gap on each side of the glass that is much larger than typical dust particles. This ensures that ripples and dimples caused by particles are no longer present. Backside pressure in each plenum is maintained by continuously supplying air into the furnace through stainless steel tubing, effectively generating uniform pressure distributions on each side of the glass. These pressure distributions serve as viscous restoring forces that correct glass shape inside a furnace and restore symmetry about the midplane, as shown in Figure 1b.

Optics for EUV, X-Ray, and Gamma-Ray Astronomy V, edited by Stephen L. O'Dell, Giovanni Pareschi,
Proc. of SPIE Vol. 8147, 81470N · © 2011 SPIE · CCC code: 0277-786X/11/$18 · doi: 10.1117/12.895413

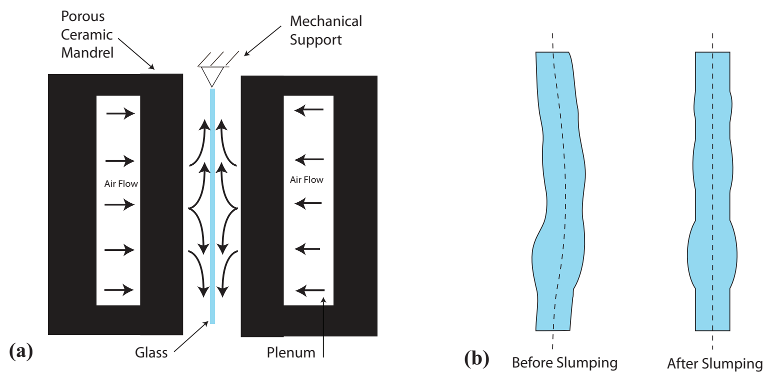

Figure 1. Schematic of the slumping process, not drawn to scale. (a) Glass sheet is vertically suspended by hooks between the mandrels, never making contact with their surfaces. Gap is much smaller than glass thickness. (b) Viscous forces drive the glass to be symmetric about its midplane.

Initial results were promising, with flatness reduced from hundreds of microns to the order of a few microns, but several sources of error were suspected to be limiting repeatability of the results.[4] Most notable is the open-loop control of process pressure, as manual mass-flow meters were used to equalize pressures during the experiment. Additionally, the larger warp observed in the direction of the gravity vector suggested that apparatus tilt could be contributing to the error. Monitoring and controlling apparatus tilt from run to run was thus suggested to improve repeatability. In this paper, we report a mathetmical model used to investigate these hypotheses to inform the design of the next generation slumping tool.

2. MATHEMATICAL MODEL

An earlier mathematical model had been developed to calculate pressure distributions on the mandrel surface for various gap sizes and supply pressures.[3] Although useful for the design of the initial slumping tool, the model was somewhat limited by its assumptions of a uniform gap across the mandrel, uniform glass thickness, and a gravity vector orientation parallel to the glass sheet. Furthermore, it only accepted two input parameters; supply pressure and gap size. In this section, we present a model capable of predicting final glass shape based on the individual pressures in each plenum, gravity vector orientation and glass thickness variation. To achieve this capability, we generalize the earlier model in order to predict pressure distributions for non-uniform gaps, as shown in 2.

2.1 Pressure Distribution Calculation

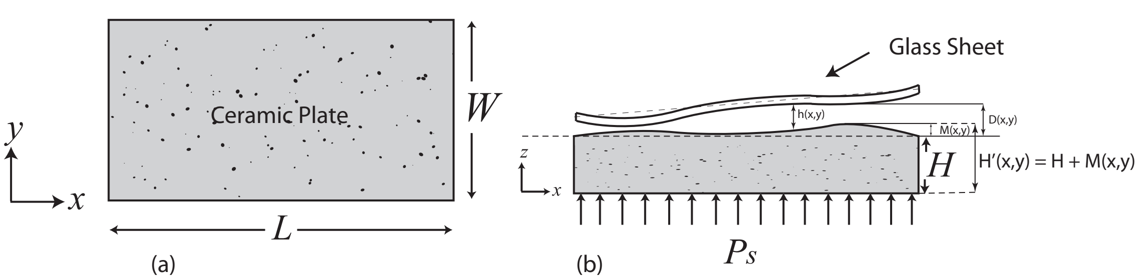

Figure 2. Air bearing with a non-uniform gap: (a) Top view. (b) Side view

Creeping flow is assumed in the porous ceramic medium, and Darcy's law is used to describe the flow according to the relation $\vec{U}' = -\frac{k}{\mu}\nabla p'$. $\vec{U}'$ is the air velocity vector field in the porous ceramic, k is the permeability coefficient, μ is air viscosity and $\nabla p'$ is the pressure gradient. Air flow is treated as an incompressible ideal gas, under steady-state conditions and isothermal throughout the medium. After applying the continuity equation, the non-dimensionalized governing equation inside the porous ceramic becomes,

$$K_x \frac{\partial^2 \tilde{p'}}{\partial \tilde{x}^2} + K_y \left(\frac{L}{W}\right)^2 \frac{\partial^2 \tilde{p'}}{\partial \tilde{y}^2} + \left(\frac{L}{H}\right)^2 \frac{\partial^2 \tilde{p'}}{\partial \tilde{z}^2} = 0, \tag{1}$$

where the dimensionless variables $\tilde{x} = x/L$, $\tilde{y} = y/W$, $\tilde{z} = z/H$, $\tilde{p}' = p'/p_a$, $K_x = k_x/k_z$ and $K_y = k_y/k_z$, where p_a is the ambient pressure and L, W and H are the length, width and thickness of the ceramic mandrel respectively, shown in Figure 2. Equation 1, coupled with the boundary conditions on the mandrel's six surfaces, allow us to deterministically predict the pressure. The mandrel's bottom surface is one of the plenum walls, and is exposed to the supply pressure P_s. The four sides of the mandrel are at atmospheric pressure conditions. The pressure boundary condition of the top surface facing the glass is more complex, and is derived from the Navier-Stokes equation by further assuming a negligible pressure gradient in the gap along the z direction. The non-dimensionalized form of the boundary condition is given by,

$$\frac{h^3 H}{12kL^2}\left(\frac{\partial^2 \tilde{p}}{\partial \tilde{x}^2} + \left(\frac{L}{W}\right)^2 \frac{\partial^2 \tilde{p}}{\partial \tilde{y}^2}\right) + \frac{3h^2 H}{12kL^2}\left(\frac{\partial h}{\partial \tilde{x}}\frac{\partial \tilde{p}}{\partial \tilde{x}} + \left(\frac{L}{W}\right)^2 \frac{\partial \tilde{h}}{\partial \tilde{y}}\frac{\partial \tilde{p}}{\partial \tilde{y}}\right) = \left(\frac{\partial \tilde{p}'}{\partial \tilde{z}}\right)_{z=H'}. \tag{2}$$

The finite differences method (FDM) is implemented to solve the coupled partial differential equations. The ceramic plate is divided in a grid of nodes, separated by distances of $\Delta\tilde{x}$, $\Delta\tilde{y}$ and $\Delta\tilde{z}$ in the x, y and z directions respectively. In order to compute the pressure distribution in the air bearing for a given gap, the two coupled partial differential equations are solved simultaneously.

2.2 Glass Shape Simulation

A MATLAB script was written to iteratively predict glass shape, according to the flow-chart in Figure 3a. Inputs to the model are glass shape $s(x, y)$, glass thickness profile $t(x, y)$, gravity vector orientation θ, glass density, mandrel-to-mandrel spacing and supply pressures (p_1 and p_2). At each step, four coupled partial differential equations (two on each side of the glass) are simultaneously solved to calculate pressure distributions on each side of the glass sheet. The sheet is divided into an array of independantly translating elements (Figure 3),

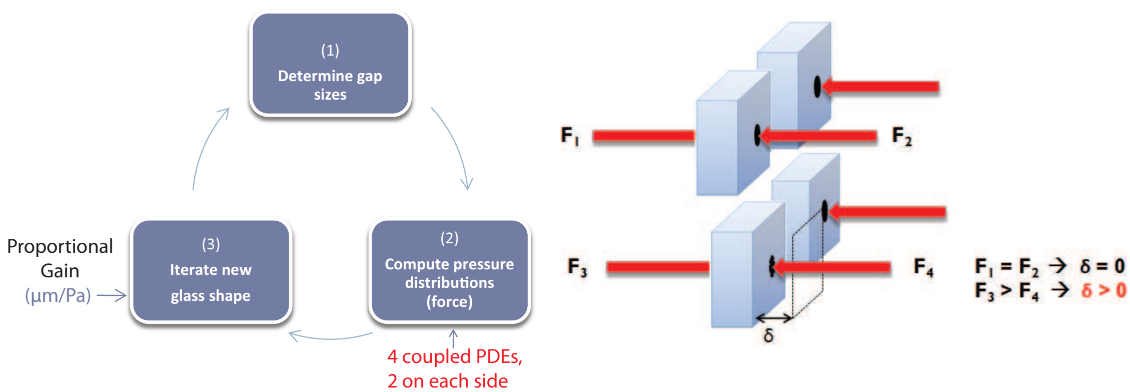

Figure 3. (a) Flowchart illustrating the iteration cycle. (b) Calculation of cell displacement in each cycle.

and the total force on the glass sheet is used to compute the new positions of individual sheet elements. The iteration cycle repeats continuously until convergence occurs when the net force on all elements falls below a defined tolerance. The translation of glass elements during each step is computed according to the equation, $z^{t+\Delta t}_{i,j} = z^t_{i,j} + \alpha \cdot (p^1{}_{i,j} - p^2{}_{i,j}) \cdot A$, where $z_{i,j}$ is the position of the element, α is a proportional gain with units μm/Pa, $p_{i,j}$ is pressure on one side of the element and A is element area. The proportional gain ensures that displacements grow smaller as net forces decrease on the path to convergence.

2.3 Results

Several simulation scenarios were chosen to provide insight into how different process parameters affect glass shape. The substrates used in the model were square sheets of Schott D-263 borosilicate glass, with a density of 2.51 gm/cm^3.[5] The effect of a pressure differential between the plenum chambers was first investigated. An assymetry in supply pressure was applied ($p_1 = 0.6 > p_2 = 0.3$ psi), and the tilt angle was set to 0°, with the objective of investigating whether unequal pressures would impart a bow on the glass and to quantify how critical is keeping equal plenum pressures. Results shown in Figure 4a suggest that bow is very small; the sheet translates 5.8 μm to a new equilibrium plane with equal pressure on both sides, with P-V variation as low as 58 nm. The glass sheet is assumed to move freely right and left during the simulation. If this is indeed the case, active pressure equalization would not be critical for achieving repeatable results.

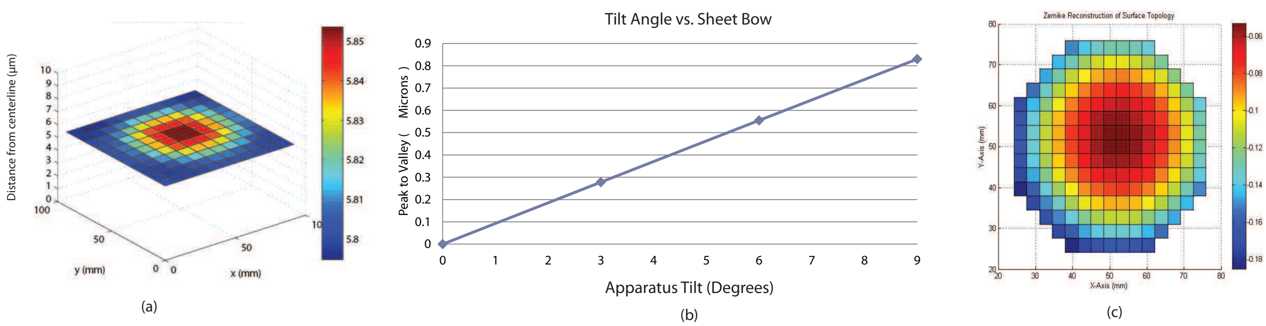

Figure 4. (a) Centerline displacement of a glass sheet due to pressure differential. Gap = 50 μm. (b) P-V bow resulting from apparatus tilt. Simulated over an area of 80×80 mm. (c) Zernike reconstruction of surface topography for 3° tilt (Z-axis in microns).

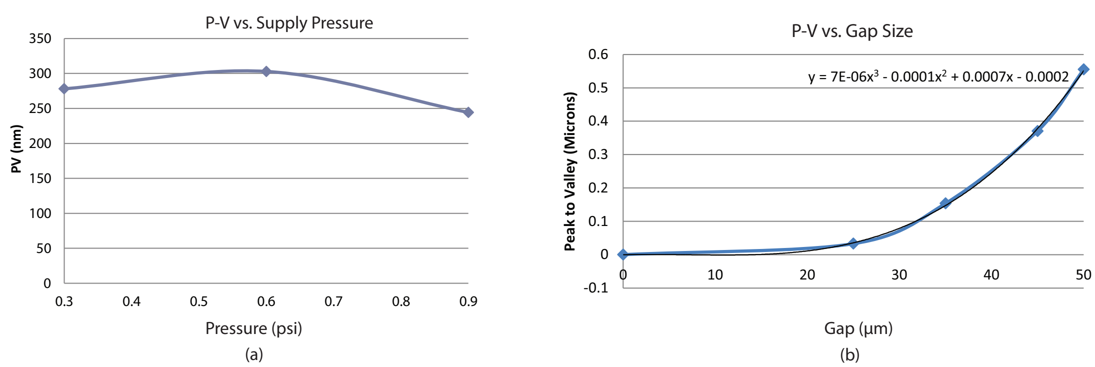

Figure 5. (a) Bow resulting from varying pressure with a constant angle. (b) Effect of varying gap size on P-V bow.

A second simulation was run to study the effect of gravity vector orientation on the sheet profile. According to the simulation shown in Figure 4b, where equal chamber pressures where assumed at different tilt angles, controlling the tilt to within 0.5° appeared to limit the bow to only tens of nanometers. Figure 4c shows a Zernike reconstruction of the computed surface topology, indicating the dominance of the Z_2^0 'defocus' term.

Given that non-zero tilt was found to cause sheet bow according to the simulation, we next studied whether increasing the pressure in both plenums equally can help reduce the bow. The simulation was run at a tilt angle of 3 degrees with equal pressures in both plenums. The set of pressures tested were $\{0.3, 0.6, 0.9\}$psi. Figure 5a shows the bow in all three cases to be equal to within 60 nm, a figure close to the computation precision of the algorithm, suggesting that tilt-induced bow cannot be reduced by increasing pressure in both chambers.

Finally, the effect of varying the gap was studied. An angle of 6° and supply pressure of 0.3 psi were chosen for this simulation, and different gap sizes were assumed between 0 and 50 μm. Figure 5b illustrates how decreasing gap size was found to reduce the P-V bow according to a 3^{rd} order polynomial. An important conclusion from this result is the desirability of being able to actively control the gap mid-process; while the initial glass warp necessitates a large gap, reducing it to only 15 μm once the glass relaxes and flattens appears to reduce gravity-induced sag significantly.

2.4 Model Verification

Experiments were conducted to examine the effect of closed-loop pressure control and controlled apparatus tilt on sheet repeatability in order to verify model predictions described in the previous section. The second generation porous air bearing tool developed by the *Space Nanotechnology Lab* was utilized for these experiments after some slight upgrades to the apparatus. Pressure control was achieved by installing two thermal-based 5000 sccm mass-flow-controllers from *MKS Instruments Inc*, used in conjuction with precision capacitance manometers with a range of 20 Torr or 0.387 psi and a resolution of 4×10^{-5} psi from the same manufacturer and LabVIEW data acquisition hardware. The angle was monitered using a digital angle measure with a 0.05° resolution from *Micro-Mark*, and adjusted using a scissor jack placed under the oven's side leg once the assembly is placed inside the furnace. Since apparatus tilt does not change during the process, measurements and adjustments were only performed once before the slump cycle begins.

As suggested by our model findings, little improvement in repeatability was observed while slumping with controlled pressure and tilt. One major unmodeled force suspected to cause y-direction variations is the hanging mechanism. In this setup of vertical slumping, the glass was vertically hung through hooks. The mathematical model assumed unconstrained motion of the glass sheet in the z direction due to pressures, but the hooks could be restricting glass motion and inducing forces that distort the sheet. The next section covers the design of a new slumping tool that aims to circumvent these problems.

3. DESIGN OF NEW SLUMPING TOOL

The main goal of the new design is to eliminate errors induced by the method used to constrain glass during vertical slumping. While experimenting with different holding mechanisms during vertical slumping could potentially solve this problem, we adopt horizontal slumping as a means to elminate it altogether. This strategy required a redesign of our slumping apparatus, and the major design challenges and solutions encountered in each subsytem are reported in this section.

3.1 Design Concept

Although earlier experiments involving horizontal slumping have been conducted at the *Space Nanotechnology Lab*, those were done using only a single air bearing.[3] This resulted in upward sheet bow due to the higher pressures at the center of the air bearing. Using a two-sided horizontal slumping tool on the other hand, would ensure identical pressure distributions on either side of the glass sheet effectively eliminating sheet bow. A further advantage of this method is that glass would be fully floating in the gap, eliminating the need for a hook that would apply reaction forces to the glass, as seen in Figure 6a. To achieve the active gap control and plate parallelism required for this design, a minimum of three degrees of freedom are required; vertical translation and two rotations. Figure 6b illustrates how this can be accomplished by actuating the top air bearing and keeping the bottom one stationary. The overall slumping apparatus, shown in Figure 7, can be divided into three systems; the sensor system, air bearing assembly and the actuation system.

3.2 Air Bearing Assembly

Ceramics have generally been the preferred material choice for air bearings since they do not oxidize in air environments and posses high stiffness and dimensional stability. The main candidates for our new apparatus were porous silicon carbide and aluminum oxide. In previous designs, the air bearing assembly -which consists of the mandrel, housing and supporting metal components- was mechanically clamped together. Since the air bearing for the new design is to be permanently bonded to achieve active gap control, the main factor informing material selection is the joining technique used to bond the mandrel and the housing.

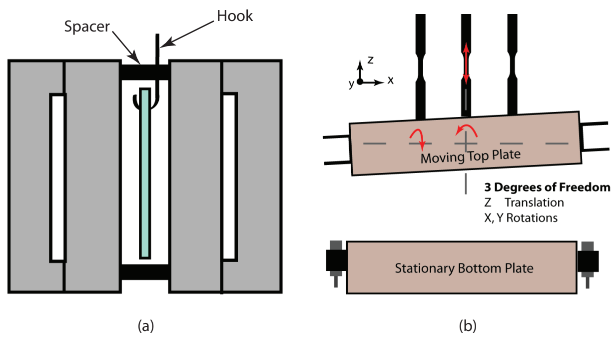

Figure 6. (a) Vertical slumping apparatus, with static mechanical spacers and hooks for hanging glass sheets. (b) New concept: Horizontal slumping with active gap control.

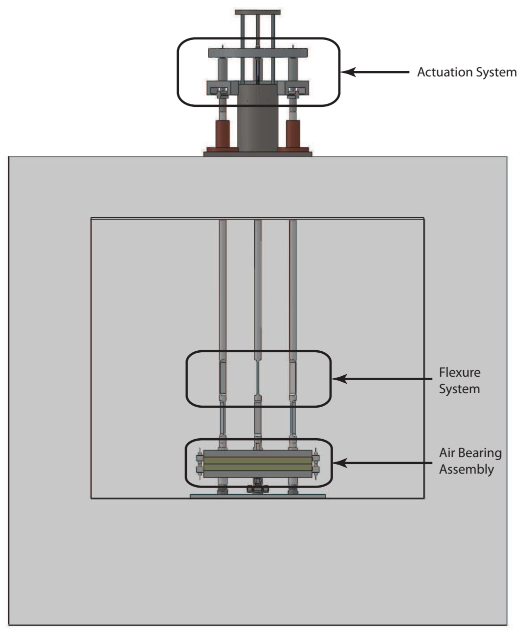

Figure 7. Overall CAD assembly of the slumping apparatus. Highlighted are the actuation system, flexure system and the air bearing assembly.

3.2.1 Joining Technique

The harsh environment inside the furnace, coupled with the CTE mismatch between ceramics and most metals make permanent bonding of the air bearing assembly a challenging task. The bond must not only be strong, but also leak-tight so that pressure can be generated in the plenum. Since nuts and bolts were found to fuse under the high temperature and the mechanical clamping force they generate loosens over time, brazing was selected as the method through which the air bearing assembly is bonded. The brazing process involves the joining of two -possibly dissimilar- materials together by heating a filler material just above its melting point. The loose-fit of both materials allows the filler to be distributed in the interface via the capillary effect, and diffuse into the materials forming a metallurgical bond often stronger than the materials being bonded, as seen in Figure 8. Generally, the melting point of the filler is above 450°C but below that of the joined materials. One advantage of brazing is that the entire assembly can be brazed at once by placing it inside the furnace and raising the temperature to above the filler's liquidus temperature, a process known as furnace brazing.

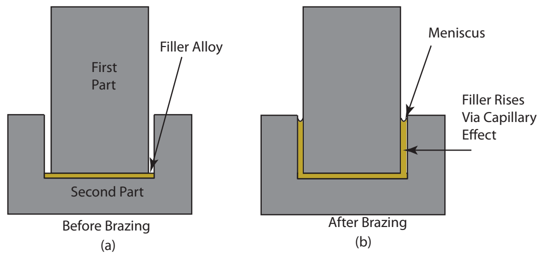

Figure 8. Illustration of the capillary effect essential to the brazing process. (a) The two parts to be bonded are loosely fitted with a filler alloy sheet (b) As the temperature rises above the filler's melting point, the capillary effect causes the filler to wick up and be distributed in the gap. As the temperature is reduced, a permanent metallurgical bond is formed.

3.2.2 Material Selection

Ceramic material choice is critical when considering brazing since not all ceramics are equally easy to braze. Of the two candidate ceramics, Aluminm Oxide was preferred for its higher CTE which facilities its brazing to certain alloys. Plates with dimensions of 12"×12"×0.75", a purity of 92%, porosity of 40% and a mean pore size of 15 μm were purchased from *Refractron Technologies Corp.* In our design, the housings of the top and bottom air bearings interface with different subsystems; the bottom air bearing must rest on a kinematic coupling at the bottom of the furnace and carry the capacitive sensors, while the top air bearing must interface with the actuation system and carry the sensor grounding plates. In order to minimize design complexity and part count, the design was carried out in a way to ensure that both the top and bottom housings were identical. The housing design can be seen in Figure 9a. Besides the brazing of two ceramic plates together, the air bearing must also

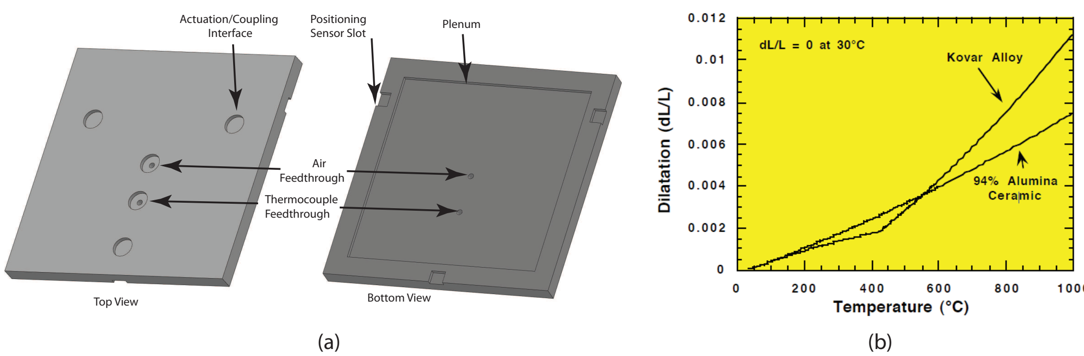

Figure 9. Strategy for positioning the air bearings: Moving top plate, stationary bottom plate.

attach to metal components such as air feed-throughs, sensor mounts and components that carry its weight. Of the different potential materials, Kovar (a Nickel-Cobalt Steel alloy) stood out as the most CTE matched material and the one most routinely used with aluminum oxide (Figure 9b). Incusil-ABA, with a solidus temperature of 605° and liquidus of 715° was selected as the filler alloy for the brazing process.

3.3 Sensor System

This system includes the different sensors used to measure plenum air pressure and temperature, as well as air bearing position. Pressure measurements are obtained by drawing a stagnant line from the oven that is connected to external pressure transducers. Temperture is measured by feeding high temperature thermocouples into the plenum. The major challenge with achieving active gap control is the need for sensors capable of withstanding temperatures reaching 570°C inside the furnace, and providing a measuring range of a few millimeters with sub-micron resolution. In order to perform these measurements, capacitive probes from *Capacitec* rated for temperatures up to 850° were purchased, shown in Figure 10a. These sensors were calibrated for operation at a maximum measuring range of 2500 μm and a resolution of 87.5 nm, ten times better than the desired posioning accuracy of 1 μm. Of the different mounting options, the threaded configuration was chosen for ease of integration with the air bearing assembly, shown in Figure 10b. For little additional cost, the manufacturer agreed to machine sensor casing from Kovar so as to thermally match it to the sensor mount.

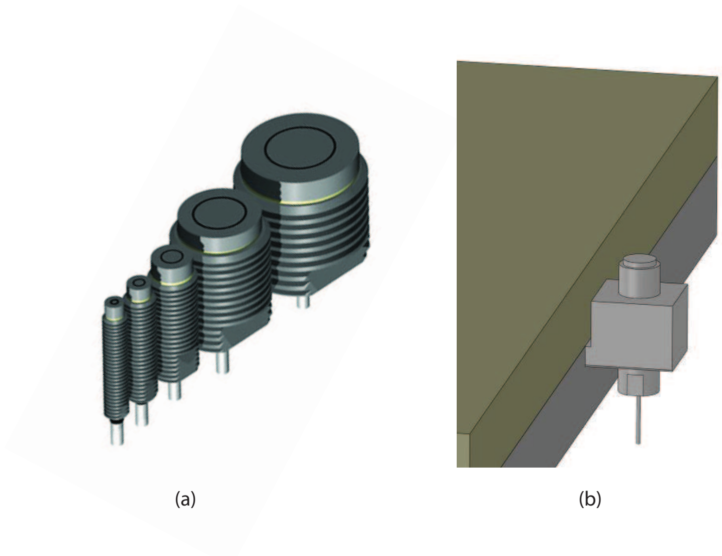

Figure 10. (a) V-series threaded capacitive probes from Capacitec, different sizes shown. (b) The threaded configuration and thermally matched Kovar material allows for easy integration into the air bearing assembly.

3.4 Acutation System

This section covers the design of the actuation system used to position the top air bearing. The objective of this actuation system is to both achieve parallelism between the air bearings and maintain the desired gap. In order to actuate the air bearing with sub-micron precision in an environment where thermal cycles between 25 to 570° C are experienced, the design of a durable and repeatable drive train is required. Pin-joints and bolts are avoided in the design to prevent backlash and fusing between different components.[6] Flexure joints were the method chosen to provide degrees of freedom to the air bearing, due to their superior repeatability, monolithic nature and ability to provide thermally symmetric designs (Figure 11a).

3.4.1 Flexure Configuration

Since the air bearing is driven by three rigid rods, flexibility must be built into the system via flexures so that the air bearing may rotate without cracking due to stresses. While this can be done in a multitude of ways, the simplest was found to be a vertical flexure configuration, where flexures are located in-line which each rod as shown in Figure 11b. The advantage of this technique is that flexures are only responsible for the air bearing's rotation, and vertical motion is achieved by simply translating the rods.

3.4.2 Coarse-Fine Actuation

The vertical flexure configuration can be actuated in a number of different ways, with a minimum number of three actuators needed to control the top air bearing's three degrees of freedom. In theory, only three linear actuators could be used to control each actuation rod independently in a single stage actuation scheme. While this technique requires the least number of actuators, it suffers from a couple of drawbacks. Most notable is a high price tag of having sub-micron resolution over the entire range of motion, when in fact it is only necessary over a few millimeters. Furthermore, the independent actuation of the three rods may induce out-of-plane forces on the air bearing that could cause cracking, making this strategy undesirable.

These problems can be avoided by using four actuators in a coarse-fine actuation scheme. In this strategy, a lower-resolution linear actuator is used to translate the entire air bearing assembly over a large range of travel.

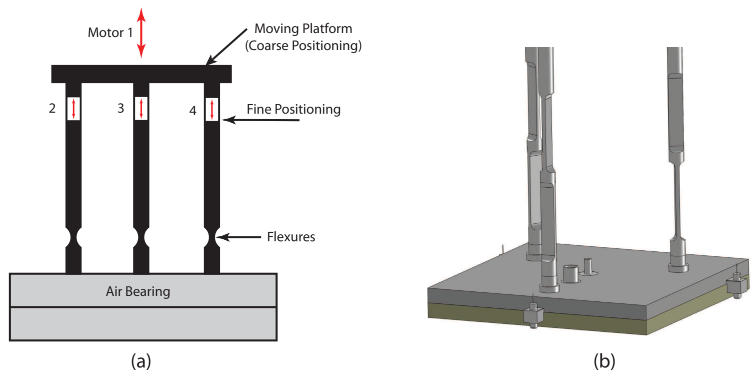

Figure 11. (a) The three driving rods are attached a common platform, which provides vertical translation. (b) Vertical flexures in-line with each rod provide the air bearing rotation.

Three high-resolution but low travel-range actuators then control the fine positioning, as shown in Figure 12. Due to its lower cost, this strategy was selected for our design. The coarse stage provides the z-translation through a

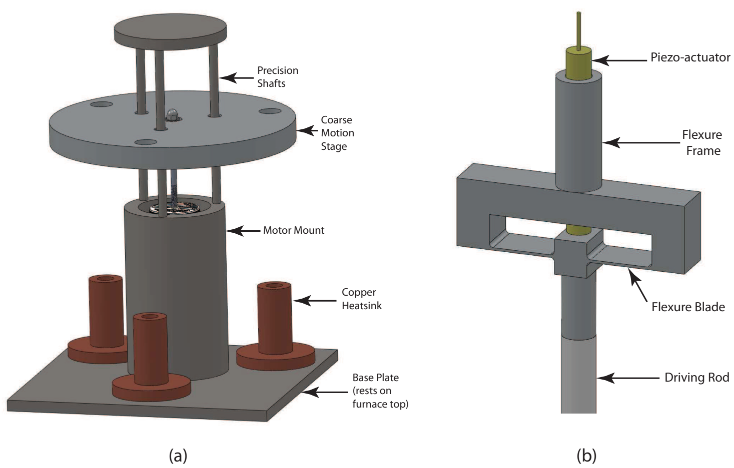

Figure 12. (a) Coarse actuation system, placed on top of the furnace. (b) Fine actuation system, placed in-line with each driving rod

23A102C stepper motor from *Anaheim Automation*, used in conjuction with a microstep driver and step motor controller from the same manufacturer. This is a hybrid stepper motor with a 6" lead-screw, providing motion at a resolution of 30 μm/step and can be micro-stepped by a factor of up to 64. The motor can also support axial loads up to 170 N. The coarse motion stage was designed around this motor for mounting on the furnace's top surface, as shown in Figure 12a. The fine positioning system is used to achieve high-resolution low-range of motion displacement to supplement the coarse actuation system. Piezo-actuators are well-suited to our need for high-resolution low range of motion and the ability to generate high forces, and are placed in-line with each driving rod. Two sets of flexures are needed for this actuation system; one to extend the length of each rod, and the other to provide rotational compliance for the air bearing while maintaining the rigidity of the driving rods. These are named the *push flexures* and the *tilt flexures* respectively, and discussed in the next section. The piezo-actuators selected were PA 100/T14 stack type piezo-actuators from *Piezosystem Jena*. They feature a range of motion of 105 μm, a resolution of 0.21 nm, and a maximum blocking force of 850 N. The sensors feature an integrated preload of 150 N, and are threaded for easy assembly into our system, as seen in Figure 12b. Ball tips avoid shear stresses that can damage the piezo. The piezo-actuators are run closed-loop with feedback from the capacitive sensors.

3.4.3 Flexure Design

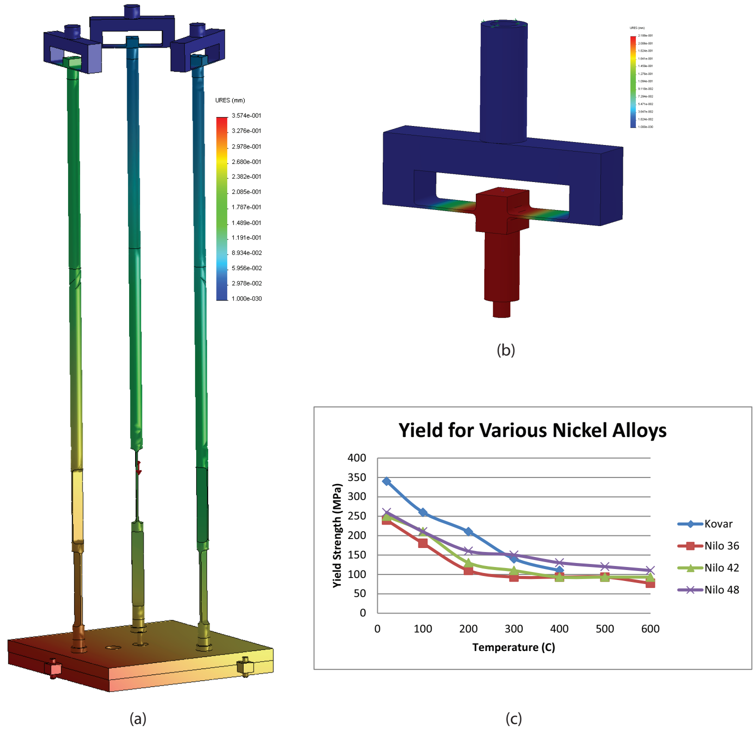

Figure 13. (a) FEA of tilt flexure. (b) FEA of push flexure. (c) Yield stress of various Ni-Fe alloys as a function of temperature.

Flexures were modeled using Bernoulli beam-bending theory, and were assumed to be thin, isotropic, and undergoing small deflections under pure moment loading $M_z(x)$. Beam deformation $y(x)$ is given by Bernoulli beam-bending theory by the expression, $\frac{\delta^2 y(x)}{\delta x^2} = \frac{M_z(x)}{EI_z}$, where E is Young's Modulus and I_z is the moment of inertia.[6,7] The equations describing flexure deformation and maximum stress are dependant on flexure geometry and boundary conditions. Given a material choice and flexure configuration, the design of flexures involves determining the three unknowns of length, width and height in the case of blade flexures. These are most often selected based on the desired deflection, maximum stress requirements and geometry considerations. In order to ensure no plastic deformation occurs in the flexure, the first constraint is defined by imposing a maximum allowable stress that is not exceed 25-35% of the material's yield stress σ_y.

3.4.4 Push Flexures

Push flexures are placed in-line with each rod and actuated by piezo-actuators to achieve vertical motion. High-strength Aluminum 7075, a material often used in flexure design, was chosen for the construction of the push flexure given its high yield strength to stiffness ratio and light weight. In order to place the piezo-actuator in-line with the driving rods, a symmetric design using two flexure blades is used as shown in Figure 12b. In this configuration, each flexure blade has clamped-guided boundary conditions with an applied end force. Equation $\delta_{max}(F) = \frac{FL^3}{12EI_z}$ is used to prescribe a deflection of 100 μm by applying a 40 N force, and Equation $\sigma_{max} = \frac{\frac{FL}{2}\frac{h}{2}}{I_z}$ applies the maximum stress constraint. The width of the flexure was constrained by the diameter of the driving rods and Aluminum plate thickness, and was selected to be 1". Calculations yielded a length of 1.5" and thickness of 0.06" as first order dimensions, which where then tested using FEA as shown in Figure 13. The flexures were manufactured by wire-EDM (electrical discharge machining) from a 1" thick Aluminum plate.[8]

3.4.5 Tilt Flexures

In order to provide the two rotational degrees of freedom for the air bearing, two layers of blade flexures are arranged according to Figure 13a. The lower layer consists of three blade flexures forming an equilateral triangle, with higher compliance for rotation around the Y-axis. The upper layer is aligned perpendicular to the lower layer, and provides higher compliance for X-axis rotation, as shown in Figure 13a. The instant centers of rotation for the bottom flexure do not intersect, and rotation about Z-axis is therefore prevented. For the upper layer, the instant centers meet at the center of the air bearing indicating the presence of parasitic degree of freedom of rotation about the Z-axis. However, since the grounding plates are twice as large as the capacitive probe sensing areas, these small rotations have no impact on displacement measurements. To select appropriate flexure dimensions, we derive the displacement and maximum stress equations for the flexure. The boundary conditions for these flexures are those of a cantilever with an end moment, since one end is free to rotate due to a moment load. The maximum rotation of the flexure tip is given by the equation, $\theta_{max} = \theta(L) = \frac{ML}{EI}$, and maximum stress by, $\sigma_{max} = \frac{Mc}{I_z}$. A rotational range of motion of 0.5° is prescribed for an applied maximum force of 50 N, and blade width is set to 0.75" as constrained by the driving rod diameter. According to Figure 13c, the yield stress of Ni-Fe alloys such as Kovar drops significantly at high temperatures, and so a conservative 90 MPa yield stress at 600°C is adopted for our design calculations. Given these requirements, the selected dimensions of the Kovar flexures were a length of 4", a height of 0.195" and a width of 0.75".

4. DISCUSSION, SUMMARY AND OUTLOOK

Results from the slumping mathematical model developed in Section 2 provided insight into how different process parameters affect glass shape. This information was used as input for the design of a third generation slumping tool, intended to solve problems experienced with the previous apparatus. The new tool will scale the process to accomodate larger flats, and conduct slumps horizontally to float the glass and minimize contact during the process. At the time of writing of this document, all components were designed and fabricated. The slumping tool assembly is partially complete, due to a delay caused by a cracked ceramic housing. Once all components are integrated, preliminary slumping experiments can be conducted with sheets of different sizes to characterize the new tool.

ACKNOWLEDGMENTS

This research project was made possible by funding from the NASA Research Opportunities in Space and Earth Sciences program (ROSES-2008). It is targeted to the Astronomy and Astrophysics Research and Analysis (APRA08) program element under the Supporting Technology category.

REFERENCES

[1] S. O'Dell, e. a., "High-resolution x-ray telescopes," in [*SPIE Conference 7803*], (2010).

[2] Akilian, M., *Thin Optic Surface Analysis for High Resolution X-ray Telescopes*, Master's thesis, Massachusetts Institute of Technology (2004).

[3] Akilian, M., *Methods of Improving the Surface Flatness of Thin Glass Sheets and Silicon Wafers*, PhD thesis, Massachusetts Institute of Technology, Department of Mechanical Engineering (2008).

[4] Akilian, M. and Schattenburg, M., "Reducing the warp of sheet glass," in [*Journal of the Society for Information Display*], (2009).

[5] America, S. N., "Characteristics of d263 thin glass," tech. rep., Available at: http://www.us.schott.com (2011).

[6] Slocum, A., [*Precision Machine Design*], Society of Manufacturing Engineers (1992).

[7] Roark, R. J., [*Roark's Formulas for Stress and Strain*], McGraw-Hill (1989).

[8] Junivall, R. C. and Marshek, K. M., [*Fundamentals of Machine Component Design*], Wiley (1999).